ELSEVIER

Polymer 42 (2001) 1547–1559

polymer

www.elsevier.nl/locate/polymer

Structure development during the melt spinning of poly(oxymethylene) fiber

J.M. Samon[a], J.M. Schultz[a,*], B.S. Hsiao[b], S. Khot[a], H.R. Johnson[a]

[a]*Department of Chemical Engineering, University of Delaware, Newark, DE 19716, USA*
[b]*Department of Chemistry, State University of New York at Stony Brook, Stony Brook, NY 11794, USA*

Received 26 April 2000; received in revised form 10 July 2000; accepted 11 July 2000

Abstract

The structural and morphological development during the melt spinning of poly(oxymethylene) was investigated via synchrotron small- and wide-angle X-ray scattering (SAXS and WAXS, respectively) techniques. Various distances from the spinneret at selected take-up speeds were examined in situ by mounting a vertically translating extruder in the synchrotron beam. The results indicate that a microfibrillar morphology is present for all cases. It is likely that the fibrils are twisted together into bundles. SAXS and WAXS patterns develop simultaneously, indicating that the fibrils develop by nucleation and growth from the amorphous melt. SAXS analysis appears to show that the long period and lamellar stack length both increase with take-up speed. The magnitude of the lamellar stack length however is grossly underestimated due to a large number of incorporated defects in the lamellar structure. The orientation of the lamellar stacks is similar to the orientation of the crystallites, showing that the macroscopic strain is transferred to the microscopic dimensions efficiently. Only at the largest take-up speed studied (850 mpm) was the influence of strain-induced crystallization seen. This was indicated by an initial decrease of crystallinity index with take-up speed at a given distance from the spinneret, followed by an increase at 850 mpm.

Keywords: Poly(oxymethylene); Fiber spinning; Structure development

1. Introduction

Poly(oxymethylene) (POM), also known as polyacetal, is a very versatile engineering plastic. According to one of its manufacturers, POM offers an excellent balance of desirable properties that bridge the gap between metals and ordinary plastics. Some of these desirable properties include high tensile strength, impact resistance, stiffness and a wide end-use temperature range. Although commonly processed by injection molding, POM also can be melt spun into fibers.

In the early 1960s the crystal structure of POM was determined to be hexagonal with unit cell parameters [1] $a = 4.47$ Å and $c = 17.39$ Å. These parameters are based on a (9/5) helical structure. Later, a more accurate (29/16) helical structure was proposed and accepted [2]. There are no fundamental differences between these models except that with this new structure the unit cell parameter c now is 56.02 Å.

The morphology of extended chain crystals of POM and of highly oriented fibers has been studied using various microscopy techniques [3–6]. Twisted bundles of microfibrils with imperfect orientation along the orientation direction [4] were seen. Superdrawn fibers were reported to have a skin–core structure [6] characterized by a double fibrillar network. Larger trunk fibrils (1 μm diameter) lying parallel to the fiber axis and a sub-network of branch fibrils (0.3 μm diameter) inside the frame. There were thin cross-fibrils (0.05 μm diameter) connected to the branch fibrils and voids between the fibrils. The density of fibrils was very high near the surface of the fiber but more porous at interior points. The morphology of highly oriented POM tapes was characterized by X-ray analysis [7]. Tapes with a low draw ratio were modeled with a two-phase system (crystalline and amorphous), while the modeling of the high draw ratio tapes required a more complicated model consisting of a three-phase system (crystalline, amorphous and oriented amorphous).

Various studies have been undertaken to investigate the effects of processing on the physical properties and structure of POM. The isothermal crystallization of POM was studied [8] and lamellar thickening was seen experimentally. The mechanism of crystal orientation in the cold drawing of compression modeled POM samples has been investigated

* Corresponding author. Tel.: +1-302-831-8145; fax: +1-302-831-1045.
E-mail address: schultz@che.udel.edu (J.M. Schultz).

0032-3861/01/$ - see front matter
PII: S0032-3861(00)00536-X

via WAXS pole figure analysis [9]. The plastic deformation was shown to follow the model of Peterlin and Meinel [10]. The effect of pressure [11] on the mechanical properties and structural characteristics of superdrawn fibers was studied. In this work a highly extended-chain structure was reported. The effect of pressurized drawing was to improve the mechanical properties by suppressing the generation of voids during drawing. Subsequent studies [12] were conducted to focus on the formation of voids, and it was shown that the void size distribution was dependent on draw ratio with high draw ratios giving rise to a greater percentage of larger voids. Also, the size of the voids was shown to dramatically alter the physical properties. Microvoids with an average cross-sectional area of less than 0.3 μm^2 had little effect on strength, but average cross-sectional area of voids beyond 1 μm^2 decreased the strength. The effect of γ-radiation [13] on the tensile properties of POM was also investigated. A strong dependence of the tensile strength and elastic modulus on radiation dose was seen. All physical properties were observed to increase with doses up to 3.88 Mrad; however a decrease of the magnitude of the properties was reported with a further increase to 7.44 Mrad.

Clark and Garber [14–17] have studied the structural development during processing of POM via physical testing, electron microscopy and X-ray analysis by the investigation of quenched samples. Blown films of POM were shown [14] to consist of a row-nucleated fibrillar morphology. Direct observation via electron microscopy revealed that these row nuclei are fibers about 200–300 Å in diameter and extended for distances up to 10 μm. These fibers are aligned in the extrusion direction and lamellae epitaxially crystallize onto these nucleating fibers. Although these nuclei themselves comprise a very small portion of the total sample volume (the remaining portion being amorphous material and lamellar crystals), they were thought to strongly influence the crystallization behavior of the sample. The development of morphology in injection molded POM bars was also investigated [16,17]. Near the mold walls highly oriented fibril nuclei surrounded by overgrowth of folded-chain lamellae formed. These fibril nuclei had a diameter of approximately 300 Å [16]. A lamellar thickness of about 160 Å was observed [17] in a sample taken near the mold wall where orientational effects were the strongest.

What is lacking in the literature is work related to the in situ investigation of the structure and morphological development during the processing of POM. This is the goal of the current research study and an on-going effort of our laboratories and other research groups. Previously, the in situ studies of the development of structure and morphology in polyethylene [18,19], poly(vinylene fluoride) [18,20], polypropylene [21,22], nylon-6 and other polyamides [23,24], polyethylene terephthalate [25,26] and polybutene-1 [27] during low and high speed melt spinning have been studied. Conflicting reports of the evolution of the small- and wide-angle X-ray scattering (SAXS and WAXS, respectively) signals have been seen and these differences are thought to be either a result of structural development or due to experimental artifacts. In some work [19,20,22], the appearance of the discrete SAXS signals before crystalline WAXS signals was observed and attributed to a spinodal decomposition-like mechanism. Still other studies [21] have observed simultaneous appearance of SAXS and WAXS scattering and a nucleation and growth mechanism can be used to explain the results. A recent study [18] by the authors have also confirmed that SAXS occurs prior to WAXS, but still conclude that the nucleation and growth mechanism can be used to explain the structural development. In this study the appearance of SAXS before WAXS was thought to be merely an experimental artifact due to the presence of very defective crystals at the onset of crystallization. At this time the long-range density fluctuations can be detected via SAXS, but on the shorter length scales examined by WAXS the crystal structure is too defective to be detected. These results are further validated by the recent work of Wang et al. [28] where the detection limit of WAXS is shown to be about 1%, whereas the detection limit for SAXS is about 0.1%.

In the present work, synchrotron X-rays were utilized to study the structural and morphological development of POM during low-speed melt-spinning using in situ SAXS and WAXS techniques. Our first goal is simply to expand the number of polymers examined in this fashion. Due the relative infancy of this technique, the number of studied polymers is small and needs to grow. Our second goal is carefully examine the data for POM and to see if it deviates from the results of the previous polymers studied. In this way we can not only expand the database of experimentally accessible polymers, but also add to the pool of notable results. It is hoped that these results, in conjunction with the results of other work, may be used to obtain a universal mechanism for basic structural development during the low-speed melt spinning of polymer fibers and the relationship between structural and morphological development and processing.

2. Experimental

2.1. Materials

The poly(oxymethylene) resin used in this study was supplied by the DuPont Company and is known commercially as "Delrin® 100". The approximate melting and glass transition temperatures of the POM sample were 180C and 0°C, respectively. The weight averaged molecular weight (M_w) was approximately 140,000 g/mol and the polydispersity index (M_w/M_n) was 1.8. Both of these results were obtained by GPC analysis.

2.2. Synchrotron characterization

This study was conducted at the Hamburg Synchrotron Radiation Laboratory (HASYLAB) in Hamburg, Germany,

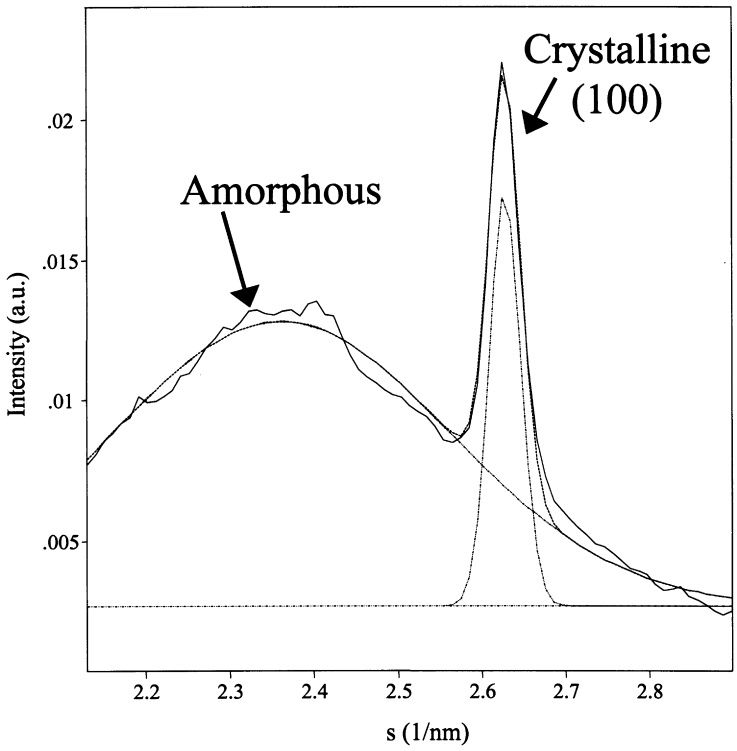

Fig. 1. Peak deconvolution of amorphous and crystalline components of the integration of the 2D WAXS pattern taken at 250 mpm and a distance of 96 cm from the spinneret.

using the polymer beamline (A2) [29]. The synchrotron radiation was monochromatized to 1.50 Å by Bragg reflection from a sagittal germanium crystal monochromator, and shaped and collimated with a cylindrical horizontal mirror in combination with a series of horizontal and vertical slit assemblies. The primary beam was rectangular in shape with approximate dimensions of 2 mm × 4 mm, with its long axis perpendicular to the fiber direction. The primary beam intensity was monitored by an ionization chamber and the intensity of the beam after passing through the sample was measured by a second ionization chamber that also acted as a beamstop. The sample-to-detector distance for the SAXS and WAXS measurements were 2314 and 106.5 mm, respectively.

The scattering patterns were corrected for fluctuations of the primary beam over time by dividing the scattered intensity with the intensity of the primary beam. All scattering patterns were also normalized for varying collection times. Finally, empty patterns of the system without a fiber sample were subtracted from the fiber patterns to correct for air and instrumental scattering.

2.3. Experimental methods and procedures

The polymer resin was extruded through a ribbon die with dimensions of 1 mm × 3 mm using a 20 mm diameter single screw extruder and a metering pump. The long axis of the polymer ribbon was normal to the direction of the incoming X-ray beam. The extruder was mounted on a platform that could be translated in the vertical direction allowing distances of 28–95 cm from the spinneret to be examined by the stationary X-ray beam. The fiber was taken up on a 19 cm godet roll whose take-up speed ranged from 50 to 850 mpm. The spinline was unstable at higher take-up speeds and any attempt to spin at a higher take-up speed resulted in fiber breakage. A small ceramic guide and roller wheel placed below the X-ray beam position was used to minimize fiber movement and vibration.

The temperature profile along the extruder was 210, 210, 220, 233 and 238°C from the feed zone to the heated spinneret block. The screw and metering pump were rotated at a constant speed of 5 and 12 rpm, respectively. Take-up speeds of 50, 250, 550 and 850 mpm were examined. At each of these take-up speeds, simultaneous two-dimensional (2D) small- and wide-angle X-ray patterns were recorded at a variety of distances from the spinneret using an imaging plate detection system. The WAXS imaging plate had a central opening of 2 cm in diameter, allowing the passage of the SAXS signals. A typical collection time for the SAXS and WAXS patterns was 3 min. After collection, the image was digitized with a resolution of 176 μm/pixel for analysis using a Molecular Dynamics imaging plate reader.

3. Data analysis techniques

3.1. WAXS

The crystallinity index (CI) was calculated by the

curve-fitting of an azimuthal integration of the fiber WAXS patterns after the empty pattern was subtracted. A typical curve fit is shown in Fig. 1. This fitting was carried out using a commercially available curve-fitting program (GRAMS32 v.4.1). Gaussian peaks were used to represent both the crystalline and amorphous contributions. The shape parameters (centroid position, full-width at half-maximum (FWHM), integral breadth) of the amorphous peak were determined from patterns taken close to the spinneret where crystallization had yet to commence. The crystallinity index, defined as the ratio of the area under the crystalline reflections to the area under the entire scattering pattern (crystalline plus amorphous), was then determined as a function of take-up speed and distance from the spinneret.

The apparent crystallite size (ACS) was estimated using the Scherrer equation [30],

$$\mathrm{ACS} = \frac{\lambda}{(\Delta 2\theta)\cos(\theta)} \tag{1}$$

where λ is the X-ray wavelength, $\Delta 2\theta$ is the integral breadth (in radians) of the crystalline peak and θ is one-half of the scattering angle, 2θ.

The crystalline orientation of the fibers was determined quantitatively by computation of the Hermans orientation factor [31] as generalized to a set of three crystallographic axes by Stein [32]. This factor is defined as

$$f_x = \frac{3\langle\cos^2\phi\rangle - 1}{2} \tag{2}$$

where $\langle\cos^2\phi\rangle$ is the averaged value of the square of the cosine of the angle ϕ between the reference direction in the sample (fiber axis) and the x-crystallographic axis. Assuming rotational symmetry about the fiber axis,

$$\langle\cos^2\phi\rangle = \frac{\int_0^{\pi/2} I(\phi)\cos^2\phi\sin\phi\,\mathrm{d}\phi}{\int_0^{\pi/2} I(\phi)\sin\phi\,\mathrm{d}\phi} \tag{3}$$

where $I(\phi)$ is the intensity reflected from the (hkl) planes which are normal to the x-crystallographic direction. Therefore f_x values can range from -0.5, when the chains are perpendicular to the x-crystallographic axis, to 1.0, when the chains are parallel to the x-crystallographic axis. When f_x equals zero, there is random orientation in the sample.

3.2. SAXS

The long period and lamellar thickness were calculated using the 1D correlation function analysis, illustrated by Strobl and Schneider [33]. In the 1D correlation function analysis it is assumed that the lamellar stacks are infinite in width and are perfectly oriented. The scattering from such a theoretical stacking would be a series of discrete peaks along the fiber direction. In actuality, this scattering due to lamellae is broadened azimuthally due to the stacks not being exactly parallel to each other (and the stack widths are finite). Therefore the scattering does not appear as discrete spots, but rather is spread over a section of the reflecting sphere in reciprocal space which area is proportional to q^2. The scattering vector, q, is defined as follows:

$$q = \frac{4\pi}{\lambda}\sin\theta \tag{4}$$

where λ is the X-ray wavelength and θ is one half the scattering angle (2θ).

A Lorentz correction is conventionally used to correct to the value that would be seen for the perfectly oriented case in the case of the extraction of a 1D meridional slice from a 2D SAXS pattern. This correction procedure was undertaken in the present study.

The correlation function is then calculated as

$$\gamma(r) = \frac{\int_0^{\infty} \bar{\imath}(q)\cos(qr)\,\mathrm{d}q}{Q} \tag{5}$$

where $\bar{\imath}(q)$ is the Lorentz corrected intensity of the extracted 1D meridional slice, q is the scattering vector defined in Eq. (4) and Q is the invariant, which is given as

$$Q = \int_0^{\infty} \bar{\imath}(q)\,\mathrm{d}q \tag{6}$$

In the present experiment the diameter of the fiber was not measured, and thus the invariant could not be corrected to take into account the effects of sample volume. This has a minimal impact because: (1) the invariant is merely used as a scaling factor and no additional conclusions are drawn based on its value; and (2) the reduction of the diameter in the region experimentally examined (28–95 cm from the spinneret) is small compared to the reduction of diameter from the spinneret to 28 cm.

The correlation function, $\gamma(r)$, is a measure of the self-correlation profile of the electron density in the lamellar stacks. The value of the first peak maximum corresponds closely with the long period. Using the method proposed by Strobl and Schneider [33], two lamellar thicknesses can be estimated from the correlation function. It is impossible from this analysis alone, however, to determine which lamellar thickness corresponds to the amorphous or crystalline thickness. Other types of data (WAXS, TEM, DSC, etc.) must be obtained to assist in the proper assignment of the lamellar thickness.

Above, the misorientation of lamellar stacks is mentioned and deserves further investigation at the present time. Longitudinal slices through the lamellar reflections in the SAXS patterns (parallel to the fiber axis) were extracted at intervals of five pixels in the lateral direction (corresponding to an interval of 0.0218°). The centroid and FWHM values of the lamellar peak in these slices were then calculated using the curve-fitting package mentioned above. The length and misorientation of the lamellar stacks with respect to the fiber axis were then estimated by a least-squares fitting of

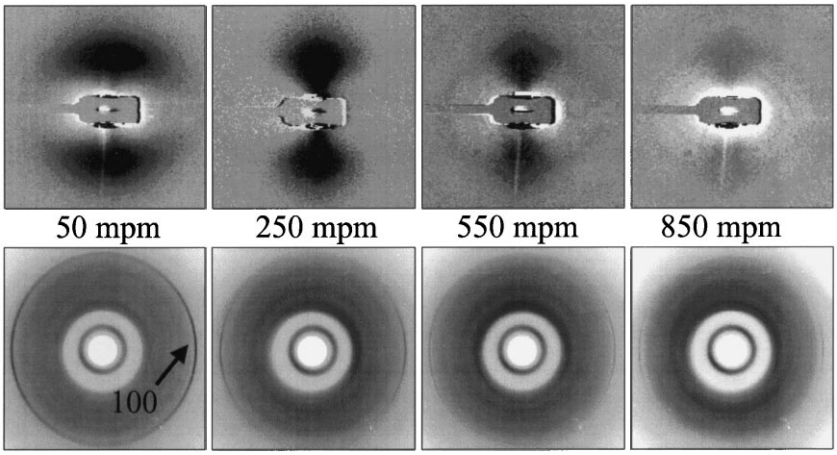

Fig. 2. SAXS and WAXS patterns taken at approximately 95 cm from the spinneret at various take-up speeds. The fiber axis is vertical.

the FWHM values as a function of scattering angle (in the lateral direction) using the following equation [34,35]:

$$\frac{\Delta z_s \cos 2\theta}{\lambda F} = \frac{1}{2l_s} + \left[\frac{1}{4l_s^2} + s^2 \sin^2 \beta_s\right]^{1/2} \quad (7)$$

where Δz_s is the FWHM of the lamellar stack in the longitudinal direction, F is the sample-to-detector distance, l_s is the length of the lamellar stack, β_s is the misorientation of the lamellar stack referenced to the fiber axis and s is equal to $q/2\pi$, where q is the scattering vector defined above. This analysis is valid only when the sample is oriented to a degree in which there in no significant arcing of the lamellar reflection. That is to say that the entire lamellar reflection must lie more or less in the lateral direction. The SAXS patterns in Fig. 2 show that this assumption is assumed to be largely valid for the present study.

As seen in this figure, the shape of the scattering in the 2D SAXS patterns varies significantly with take-up speed, with a substantial broadening of the lamellar reflections in the lateral direction for the case of low take-up speed. The lateral width of the lamellar reflection is related to the widths of small-angle scattering entities (diameters of single fibrils or bundles of fibrils) and the degree of misorientation. We have used two independent methods to estimate the lateral width of the scattering entity from SAXS data. First, a Guinier-type analysis [30] was conducted on the lamellar reflection by the extraction of a 1D slice running along the lateral direction at the scattering angle maximum intensity of the lamellar reflection. The lateral size of the lamellae were evaluated via the following equation:

$$I = I_0 \exp\left(-\frac{q^2R^2}{4}\right) \quad (8)$$

where I/I_0 is the measured intensity as a function of q and R is the radius of the rod-like scattering entity (in the present case fibrils). The radius can easily be determined from the slope of a plot of the natural logarithm of (I/I_0) versus q^2 in the low q range between zero and 0.0102 Å^{-1}. Secondly, this lateral slice of the lamellar reflection was curve fit with a single Gaussian peak to find its peak shape parameters (centroid position and integral breadth). These parameters were used to find the lateral dimension of the scattering entity using the Scherrer equation (Eq. (1)) after correcting for broadening due to misorientation of the lamellae. We acknowledge that the second method is quite crude, as the Scherrer equation may not be justified here, but it provides us a measure to check the results from the Guinier analysis.

The experimental integral breadth of the lamellar reflection in the lateral direction (β_{exp}), was broken down into its components, the integral breadth due to misorientation (β_1) and the lateral breadth due to the lateral size of the SAXS scattering entity (β_2) via the following equation:

$$\beta_{exp}^2 = \beta_1^2 + \beta_2^2 \quad (9)$$

The first term on the right-hand side was calculated from the degree of misorientation found from Eq. (7) and β_2 was then determined and used in the Scherrer equation to estimate the lateral size in the absence of any misorientation induced broadening.

4. Results and discussion

4.1. Qualitative analysis of X-ray patterns

The SAXS and WAXS patterns in Fig. 3 are in situ images recorded at two different distances from the spinneret, namely 49.5 and 52.5 cm, for a take-up speed of 50 mpm. At a position of 49.5 cm from the spinneret a purely amorphous WAXS pattern is seen along with no discrete scattering in the SAXS regime. In addition, there was no diffuse SAXS scattering detected at this time. At 52.5 cm both crystalline WAXS scattering and discrete meridional SAXS scattering is observed. The results at this take-up speed and all other take-up speeds examined show that the SAXS and WAXS patterns probably develop simultaneously, and at no time do SAXS images appear

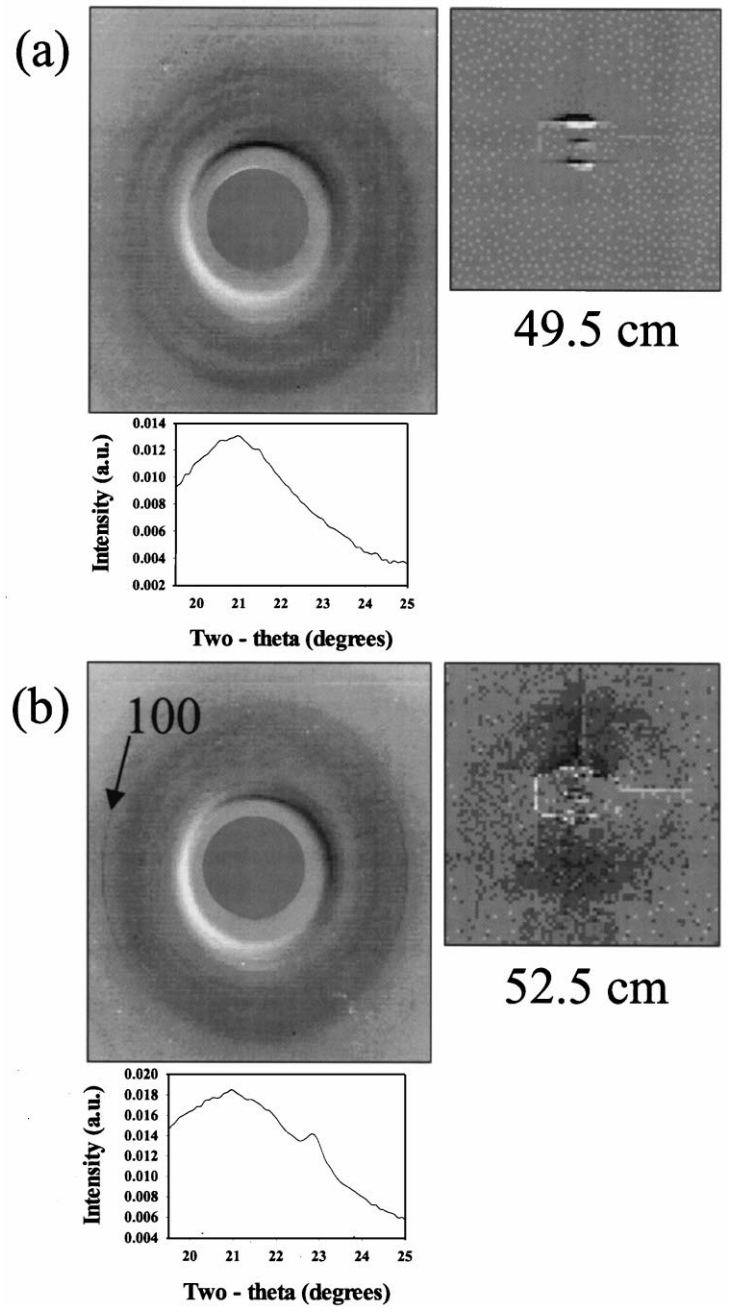

Fig. 3. In situ SAXS and WAXS patterns taken at (a) 49.5 cm and (b) 52.5 cm from the spinneret at a take-up speed of 50 mpm. An azimuthal integration of the WAXS pattern is also shown. The fiber axis is vertical.

before WAXS images. According to literature values [36] the average densities of the crystalline and amorphous phases of POM are 1.504 and 1.261 g/cm^3, respectively. This is of concern because the SAXS scattering intensity is proportional to the square of the density difference between the crystalline and amorphous phases. These results discount the possibility that spinodal decomposition of the amorphous melt is occurring, as one of the requirements is the appearance of long range density fluctuations prior to the development of crystalline. If in fact this was occurring, discrete or diffuse SAXS scattering would appear before crystalline WAXS reflections. Thus, the nucleation and growth mechanism is suggested as the dominant mechanism governing the initial development of structure.

Fig. 2 again shows 2D SAXS and WAXS patterns taken at a distance of approximately 95 cm from the spinneret for each of the take-up speeds examined. In examining the SAXS patterns, the lateral broadening of the lamellar peaks is apparent as well as the decrease of this broadening with the increase in take-up speed. The intensity of the lamellar reflection also decreases with increased take-up speed (possibly a result of the decrease in fiber diameter).

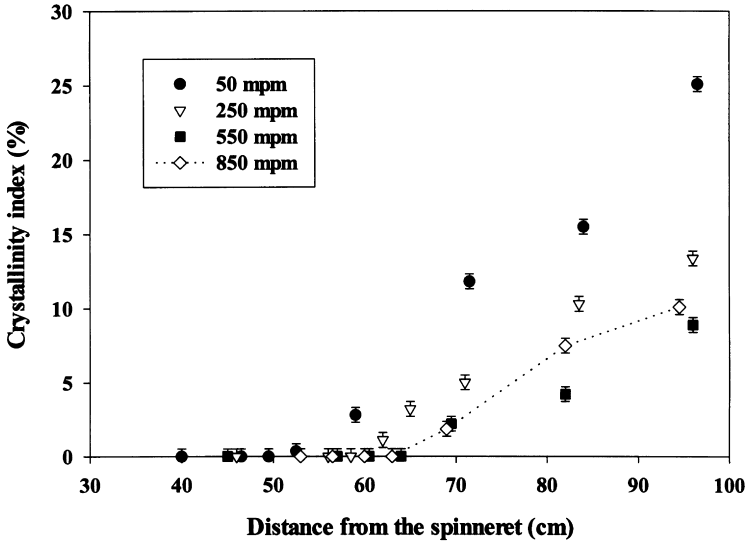

Fig. 4. Crystallinity index as a function of take-up speed and distance from the spinneret.

The lack of any equatorial scattering for all take-up speeds is noted, and will be discussed in more detail below. The near vertical light line appearing in the bottom half of the SAXS patterns (50, 550 and 850 mpm) is a data artifact resulting from a scratch on the imaging plate and should be ignored.

In examination of the WAXS patterns only a single equatorial reflection was recorded. This result was consistent for all take-up speeds examined. This equatorial peak results from the (100) reflecting plane of POM. The increase of crystalline orientation with take-up speed is also evident with the decreased azimuthal spread of the crystalline reflection. The isotropic ring appearing near the center of the imaging plate is a result of scattering from Kapton® polyimide film placed over the vacuum windows, and is not relevant in any further discussion.

4.2. Crystallinity index

Fig. 4 shows the crystallinity index (CI) as a function of take-up speed and distance from the spinneret. At a distance of 50 cm along the spinline, only amorphous scattering is observed for all take-up speeds. Further along the spinline at a distance from the spinneret which is dependent on the take-up speed, crystallinity develops and subsequently increases. Increasing from 50 to 550 mpm results in a depression of the crystallinity at a given distance from the spinneret and the first indication of crystallinity appearing at distances further from the spinneret. At 850 mpm the trend reverses and crystallinity develops at a distance on the spinneret above that at which crystallinity develops for 550 mpm. The CI at a given distance is also found to be greater for 850 mpm than for 550 mpm.

In the spinning of polymer fibers there are competing polymer crystallization effects. In the absence of appreciable strain, the crystallization kinetics are mainly controlled by the time a volume element spends in the temperature range in which crystallization kinetics are large. In fiber spinning this time depends on the take-up speed and the rate of cooling of the fiber. With increasing take-up speed this time decreases and so does the level of crystallinity. In the presence of large strain rate the crystallization kinetics are now controlled not only by time, but also by the behavior of orientation-induced crystallization. In this case, the large strain rate can accelerate the rate of crystallization as take-up speed is increased. The critical point at which orientation-induced crystallization becomes significant has been described by Keller and Kolnaar [37], and is a function of the strain rate and the molecular weight distribution of the polymer. In short, the theory states that there is a critical molecular weight for a given strain rate and all chains possessing a greater molecular weight will be stretched in an elongational force field. These chains are oriented along the direction of the deformation and will not have sufficient time to relax after the force field is removed. As the strain rate increases, the critical molecular weight decreases, allowing a larger fraction of the polymer chains to be stretched. These oriented chains can crystallize into extended chain crystals, known as shish structures, with a significantly faster rate.

The present results suggest that as take-up speed is increased to 850 mpm, a point is reached at which there is a significant number of polymer chains over the critical molecular weight, allowing orientation-induced crystallization to become the dominant factor affecting the crystallization kinetics. At take-up speeds below 850 mpm, due to the smaller strain rates, the effects of orientation-induced crystallization are minimal and the overall kinetics are primarily affected only by the time spent in the crystallizable temperature range.

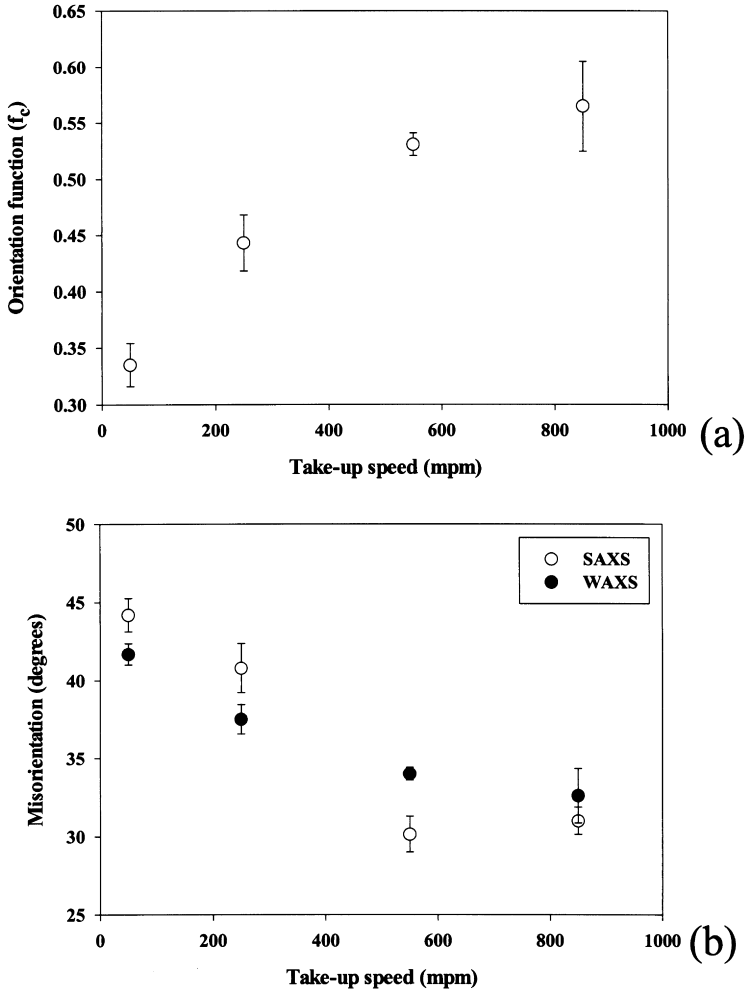

Fig. 5. (a) Crystalline orientation function as a function of take-up speed for the on-line samples calculated from the (100) reflection in the WAXS data. (b) Misorientation in degrees of the lamellar stacks and of the crystallites as a function of take-up speed.

4.3. Crystallite and lamellar stack orientation

Fig. 5(a) shows the average Herman's orientation function calculated from the (100) reflection of WAXS for each take-up speed. The orientation functions were found not to vary with distance from the spinneret for a given take-up speed. The average value and the error bar were determined from the mean and standard deviation of the orientation function values determined at each position along the spinline for a given take-up speed. Fig. 5(b) shows the misorientation of the lamellar stacks (from SAXS) as a function of take-up speed, as determined by Eq. (7). Also shown in Fig. 5(b) is the misorientation of the crystallites as determined by applying the results shown in Fig. 5(a) to Eq. (2). As take-up speed increases, the degree of misorientation of the lamellar stacks and the crystallites decrease, and thus both become more oriented with the fiber axis. These misorientation values are with respect to the fiber axis. It is noted that the orientation of the lamellar stacks is quite similar to the orientation of the crystallites. This result has also been seen in fibers of nylon-6 [34] and polyethylene [35].

4.4. Morphological structure

Fig. 6(a) shows the apparent lamellar stack length as calculated by the least-squares fitting of Eq. (7) with the extracted SAXS data. The figure illustrates that as the take-up speed is increased the apparent lamellar stack's length also increases. Fig. 6(b) shows the lateral dimension of the lamellar entity as calculated from the Scherrer equation using the crystalline WAXS data. Also shown in this figure is the lateral size as calculated from the integral breadth of the lamellar reflection extracted from the SAXS data after being corrected for misorientation-induced broadening, as well as from the Guinier analysis of the SAXS lamellar reflection. The lateral sizes calculated from the use of the Scherrer equation on the SAXS data are comparable to those calculated from the Guinier analysis of the SAXS data. Both of these values are always greater than that of the lateral size found from the use of the Scherrer equation on the WAXS data. The three data sets however follow a similar trend, with increasing take-up speed causing an increase in the lateral size of the scattering entity. It should be noted that the WAXS ACS

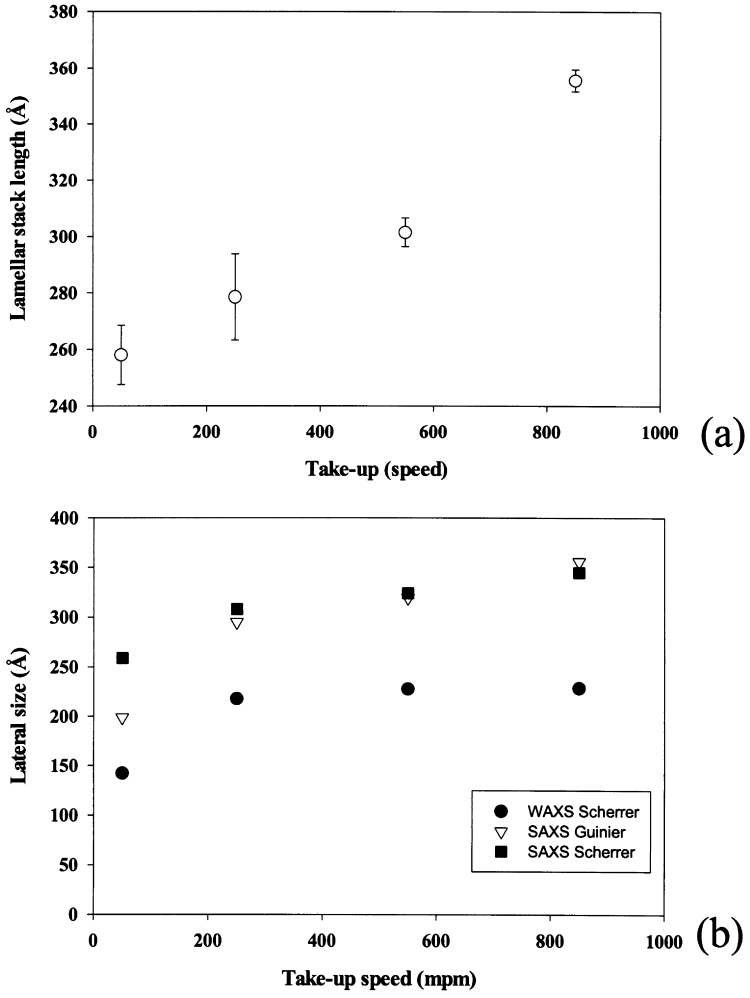

Fig. 6. (a) Length of the lamellar stacks calculated from the SAXS data as a function of take-up speed. (b) Diameter of the lamellar scattering entity as a function of take-up speed calculated from SAXS and WAXS data.

calculation finds the average lateral dimension of the crystallites, which is very sensitive to the effects of crystal defects, while the SAXS ACS calculation finds the average lateral dimension of the lamellar entity, which does not depend on the crystal defects. The SAXS Guinier calculation also estimates the lateral size of the lamellar entity, but is usually weighted to larger sizes due to the analysis only on small q values. With this in mind, the size distribution of the three methods of analysis is logical at each take-up speed, with the WAXS ACS giving the smallest size, heavily skewed by the crystal imperfections.

As one might notice in the above discussion the term lateral dimension of the lamellar entity is used in place of fibrillar diameter. From the lateral sizes determined it is thought that the result may be too large to be the diameter of one fibril, but rather an aggregation or bundle of fibrils. If such a bundle exists, a single fibril diameter cannot be resolved and only the diameter of the fibrillar bundle is found. Bundles of microfibrils have been observed via AFM [3,4] and SEM [5] in extended chain fibrillar crystals of POM, as well as in blown films of POM [14]. From this work the bundles appeared to be comprised of fibrils that are twisted together. This twisting of the fibrils in a bundle might explain why individual fibrillar diameters could not be extracted from the X-ray analysis. The lateral dimension found from the present experiment correspond closely with those found during examination of blown films of POM [14]. As the processing conditions for the film blowing were not mentioned in the cited reference, direct processing-structure comparisons cannot be made here. The lateral dimension of these bundles of microfibrils increases with take-up speed. This is likely due to the effect of an increased fibril nucleation rate with increasing elongational strain. The higher density of fibrils should translate into a higher probability of bundling. In addition it has been illustrated above that with an increased take-up speed the orientation of the crystalline polymer chains increases with respect to the fiber axis. If it were assumed that the probability that two adjacent fibrils can bundle increases if they have similar crystalline orientation, then as the distribution of orientations becomes less wide, which occurs as take-up speed increases, the probability of bundling would increase.

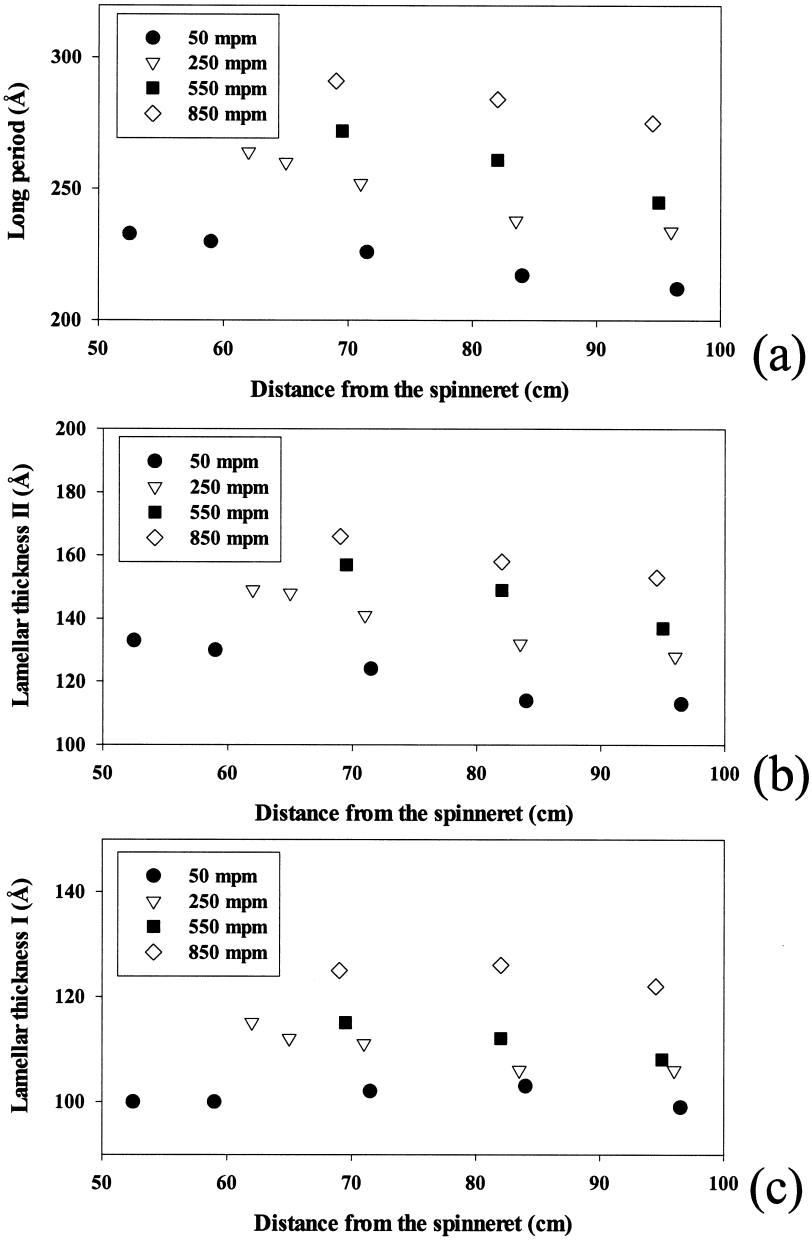

Fig. 7. Results of the correlation function analysis showing (a) long period; (b) lamellar thickness I; and (c) lamellar thickness II as a function of take-up speed and distance from the spinneret.

Fig. 7 illustrates the results of the correlation function analysis showing the average values of long period and lamellar thicknesses from the 1D meridional SAXS scan. The largest long period and lamellar thicknesses are found at the highest take-up speeds and vice versa. It is thought that lamellar thickness I probably corresponds to the crystalline lamellae while lamellar thickness II corresponds to the amorphous lamellae. This can be justified by comparing the results shown in Fig. 8 to the results shown in Fig. 4. Fig. 8 shows the possible linear crystallinity (lamellar thickness/long period) for both lamellar thicknesses as functions of take-up speed and distance from the spinneret. Similar trends are seen in the case of lamellar thickness I being assigned as the crystalline thickness (Figs. 8(a) and 4): (1) the crystallinity generally increases with the distance from the spinneret; and (2) a decrease in the crystallinity as take-up speed increases from 50 to 550 mpm and then a subsequent increase at 850 mpm. If lamellar thickness II were used as the crystalline thickness no such trends can be seen. The magnitude of the linear crystallinity does not correspond directly with the crystallinity index found from WAXS analysis because the 1D meridional slice extracted for the correlation function analysis does not properly represent the SAXS scattering due to the large lateral breadth of the lamellar peaks. Both the long period and amorphous thickness decrease slightly as one travels away from the

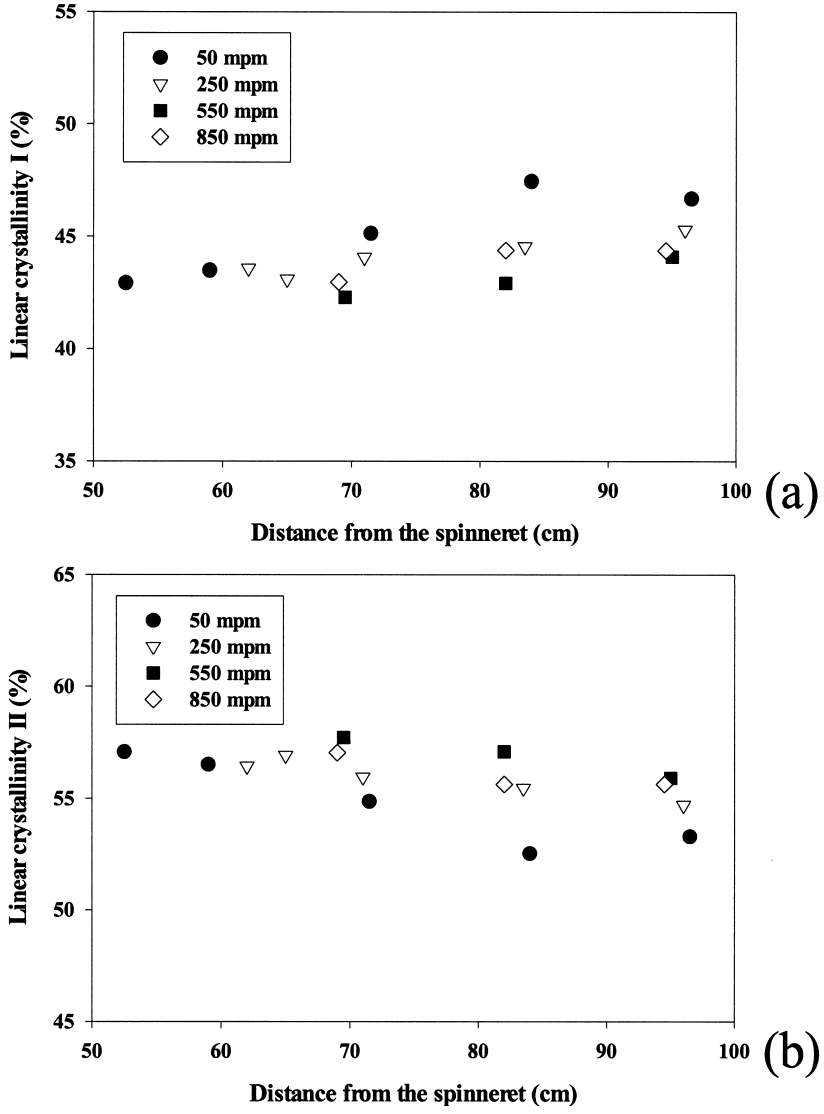

Fig. 8. Linear crystallinity as calculated from (a) lamellar thickness I and (b) lamellar thickness II shown in Fig. 6. Lamellar thickness I is thought to represent the crystalline thickness.

spinneret for all take-up speeds. This is possibly a result of space-filling crystallization taking place along the spinline, producing a thinner population of crystallites between the existing lamellae.

The quantitative similarities between the magnitude of the long period calculated via the correlation function analysis and the lamellar stack length as estimated by Eq. (7) must be addressed. Clearly, the lamellar stack length should be significantly larger than the long period. As there are no large errors in computation, another reason is sought to validate the apparently erroneous results. The possibility of broadening the SAXS reflections in the meridional direction due to defects or imperfections in the lamellar stacking must be examined closely, as this would cause errors in the lamellar stack length calculated via Eq. (7), namely a gross underestimation of the stack length. As the driving force for crystallization is quite substantial and the time period for crystallization is quite short it is not unreasonable to assume that crystallizing polymer chains do not possess much mobility during the crystallization process. Therefore, many defects can be incorporated into the lamellar morphology and stacking.

These deviations can result in disorder of the second kind [30]. A crystal lattice disorder of the second kind means that there is a lack of long-range order within the crystal. The distance between nearest neighbors always fluctuates to a small degree, but the fluctuations increase in amplitude as the number of intermediate atoms increase. This kind of distortion can be extrapolated to the larger length scales probed by SAXS. Instead of individual atoms fluctuating in their position, the individual lamellae themselves, which are contained in the microfibrils, can have non-identical thicknesses and can be irregularly spaced with respect to each other. This type of disorder manifests itself in the

SAXS pattern as: (a) no broadening of the relnode at the origin (no scattering about zero angle); and (b) sequential broadening of meridional relnodes (often making second and higher order relnodes indistinguishable form the background). In contrast if the meridional broadening were due to statistics of the stack length itself, the broadening would not only be apparent in the first-order peaks, but would also be observed about the origin and in higher order peaks. The latter phenomenon is not detected in the present case, and therefore the influence of stack length may be minimal. The effects of these lamellar stack imperfections is illustrated in the work of Bonart and Hoseman [38] where a model consisting of lamellar stacks containing lamellar stacking disorder was used to predict a diffraction pattern similar to the patterns observed presently. Additional work on the modeling of the incorporation of defects and the affects of these defects on the diffraction patterns is treated by Hoseman and Bagchi [39]. This work shows similar results, substantial meridional broadening of the first-order SAXS peak resulting from defective lamellar stacking.

There is a notable absence of any observable equatorial SAXS streak in the recorded SAXS patterns. Scattering along the equator could possibly arise from the presence of voids elongated along the fiber axis or of the presence of longitudinally aligned entities (fibrils). The possibility of the presence of voids is eliminated if in fact no equatorial scattering is observed, although the assumption of the presence of fibrils is assumed to hold true based on the results discussed above. Therefore a hypothesis on how there could be an absence of observable diffuse scattering on the equator in the presence of fibrils must be conjectured.

At least two possibilities exist to explain the presence of axial fibrils without any equatorial scattering signal being observed. First, it is suggested that the fibrils do not scatter as individual entities but as composite twisted bundles made up of many fibrils. This aggregation effectively eliminates the presence of scattering entities with small diameters, and only entities with a large lateral dimension remain. In reciprocal space these large diameter bundles of fibrils would scatter in a region of *q*-space on the equator very close to the beamstop. The *d*-space limit of the beamstop in the equatorial direction is approximately 495 Å in this study. With this in mind, an examination of the SAXS patterns in Fig. 2 show that the width of the lamellar reflection is on the order of the width of the beamstop. Therefore, it is a distinct possibility that there possibly is an equatorial streak present which wholly resides in the portion of *q*-space behind the beamstop. The second possibility is that the molecular packing in the fibrils is very defective, providing little electron density difference between the fibril and the amorphous matrix that surrounds it. This suggestion is in line with previous work [18,23,27] showing that the initial structure that is observed on-line during the melt spinning process is highly defective fibrils.

5. Conclusions

The structural and morphological development during the melt spinning of POM was studied using in situ small- and wide-angle X-ray scattering techniques. There appears to be a microfibrillar microstructure present at all take-up speeds, which is in line with the published results on PE, PVDF, nylon-6 and PB1. These fibrils can be thought of as the initial shish structures (extended chain crystals) of a shish-kebab type morphology before any kebab growth (folded chain crystals) occurs. The simultaneous appearance of the discrete SAXS and crystalline WAXS reflections further substantiate the nucleation and growth mechanism of shish-kebab formation. The dimensions of this microstructure are dependent on the strain rate applied during fiber formation. Larger strain rates (or take-up speeds) give rise to longer values of lamellar stack length and long period as well as an increase in the lateral width of the fibrillar entity. The magnitude of the lamellar stack length is thought to be clouded by the meridional broadening introduced by defects of the second kind in the lamellar stacking. The increase of lateral width may be a result of a coalescence of adjacent fibrillar bundles. Larger strain rates also promote orientation of both lamellar stacks and crystallites with respect to the fiber axis. The lamellar orientation appears to be similar to that of the crystallite orientation. At the highest strain rate studied the effects of orientation-induced crystallization begin to dominate the crystallization kinetics. As crystallization progresses during spinning, both the crystalline and amorphous thicknesses decrease as a volume element travels away from the spinneret. This is likely due to a space-filling crystallization of a thinner population of crystallites between the existing lamellae.

Acknowledgements

The authors would like to thank the NSF-GOALI program (DMR-9629825) for financial support. The authors would also like to thank Dr B.B. Sauer of DuPont for generous donation of the poly(oxymethylene) used in this study. Dr A. Meyer and R. Dohrmann of DESY were vital in the experimental set-up and experimental preparations.

References

[1] Tadokoro H, Yasumoto T, Murahashi S, Nitta I. J Polym Sci 1960;44:266.
[2] Carazzolo GA. J Polym Sci A 1963;1:1573.
[3] Snétivy D, Vancso GJ. Colloids Surf A 1994;87:257.
[4] Vancso GJ, Nisman R, Snétivy D, Schönherr H, Smith P, Ng C, Yang H. Colloids Surf A 1994;87:263.
[5] Snétivy D, Vancso GJ. Macromolecules 1992;25:3320.
[6] Komatsu T. J Mater Sci 1993;28:3043.
[7] Jungnitz S, Jakeways R, Ward IM. Polymer 1986;27:1651.
[8] Yeh F, Hsiao BS, Chu B, Sauer BB, Flexman EA. J Polym Sci: Polym Phys 1999;37:3115.
[9] Schweizer T, Vancso G. Angew Makromol Chem 1989;173:85.

[10] Peterlin A, Meinel G. Makromol Chem 1971;142:227.
[11] Komatsu T, Enoki S, Aoshima A. Polymer 1991;32:1988.
[12] Komatsu T, Enoki S, Aoshima A. Polymer 1992;33:2123.
[13] Patell YR, Schultz JM. J Macromol Sci Phys 1973;B7:445.
[14] Garber CA, Clark ES. J Macromol Sci Phys 1970;B4:499.
[15] Clark ES, Garber CA. Int J Polym Mater 1971;1:31.
[16] Clark ES. Appl Polym Symp 1973;20:325.
[17] Clark ES. SPE J 1967;23:46.
[18] Samon JM, Schultz JM, Hsiao BS, Seifert S, Stribeck N, Gurke I, Collins G, Saw S. Macromolecules 1999;32:8121.
[19] Katayama K, Amano T, Nakamura K. Kolloid Z Z Polym 1968;226:125.
[20] Cakmak M, Teitge A, Zachmann HG, White JL. J Polym Sci: Polym Phys 1993;31:371.
[21] Kolb R, Seifert S, Stribeck N, Zachmann HG. Polymer 1999;41:1497.
[22] Ryan AJ, Fairclough PA, Terrill NJ, Olmsted PD, Poon WCK. Faraday Discuss 1999;112:13.
[23] Samon JM, Schultz JM, Hsiao BS, Wu J, Yeh F, Kolb R. J Polym Sci: Polym Phys 1999;37:1277.
[24] Hsiao BS, Barton Jr. R, Quintana J. J Appl Polym Sci 1996;62:2061.
[25] Hirahata H, Seifert S, Zachmann HG, Yabuki K. Polymer 1996;37:5131.
[26] Kolb R, Seifert S, Stribeck N, Zachmann HG. Polymer 2000;41:2931.
[27] Samon JM, Schultz JM, Hsiao BS, Wu J, Khot S. J Polym Sci: Polym Phys 2000;38:1872.
[28] Wang ZG, Hsiao BS, Sirota EB, Agarwal P, Srinivas S. Macromolecules 2000;33:978.
[29] Elsner G, Riekel C, Zachmann HG. Adv Polym Sci 1985;67:1.
[30] Guinier A. X-ray diffraction in crystals, imperfect crystals, and amorphous bodies. San Francisco, CA: Freeman, 1963.
[31] Hermans JJ, Hermans PH, Vermeas D, Weidinger A. Rec Chim Trav 1946;65:427.
[32] Stein RS. J Polym Sci 1958;31:327.
[33] Strobl GR, Schneider M. J Polym Sci: Polym Phys 1980;18:1343.
[34] Murthy NS, Bednarczyk C, Moore RAF, Grubb DT. J Polym Sci: Polym Phys 1996;34:821.
[35] Grubb DT, Prasad K. Macromolecules 1992;25:4575.
[36] Miller RL. In: Brandrup J, Immergut EH, Grulke EA, editors. Polymer handbook, 4th ed. New York: Wiley, 1999. p. VI-56.
[37] Keller A, Kolnaar HWH. Materials science and technology: a comprehensive treatment, vol. 18. Weinheim: VCH, 1997 (chap. 4, p. 190).
[38] Bonart R, Hosemann R. Kolloid-Z 1962;186:16.
[39] Hoseman R, Bagchi SN. Direct analysis of diffraction by matter. New York: Interscience, 1962 (p. 318).